FEBRUARY 07 2019

Rules-of-thumb to design a uniform spherical array for direction finding—Its Cramér–Rao bounds' nonlinear dependence on the number of sensors

Kainam Thomas Wong; Zakayo Ndiku Morris; Chibuzo Joseph Nnonyelu

J. Acoust. Soc. Am. 145, 714–723 (2019)
https://doi.org/10.1121/1.5088592

Rules-of-thumb to design a uniform spherical array for direction finding—Its Cramér–Rao bounds' nonlinear dependence on the number of sensors

Kainam Thomas Wong,[1,a)] Zakayo Ndiku Morris,[2] and Chibuzo Joseph Nnonyelu[3]
[1]*School of General Engineering, Beihang University, Beijing, China*
[2]*Department of Electronic and Information Engineering, Hong Kong Polytechnic University, China*
[3]*Department of Electrical Engineering, University of Nigeria, Nsukka, Enugu State, Nigeria*

(Received 22 August 2018; revised 3 January 2019; accepted 11 January 2019; published online 7 February 2019)

This paper discovers rules-of-thumb on how the estimation precision for an incident source's azimuth-polar direction-of-arrival (ϕ,θ) depends on the number (L) of identical isotropic sensors spaced uniformly on an open sphere of radius R. This estimation's corresponding Cramér–Rao bounds (CRB) are found to follow these elegantly simple approximations, useful for array design: (i) For the azimuth arrival angle: $2\pi(R/\lambda)(\sigma_s/\sigma_n)\sqrt{2LM\mathrm{CRB}(\phi)}\sin(\theta) \approx (Le^{1/14})^{-1} + \sqrt{3} \underset{L\to\infty}{\longrightarrow} \sqrt{3}$, $\forall(\phi,\theta)$; and (ii) for the polar arrival angle: $2\pi(R/\lambda)(\sigma_s/\sigma_n)\sqrt{2LM\mathrm{CRB}(\theta)} \approx \sqrt{3} - (Le^{6/7})^{-1} \underset{L\to\infty}{\longrightarrow} \sqrt{3}$, $\forall(\phi,\theta)$. Here, M denotes the number of snapshots, λ refers to the incident signal's wavelength, and $(\sigma_s/\sigma_n)^2$ symbolizes the signal-to-noise power ratio.
 https://doi.org/10.1121/1.5088592

[ZHM] Pages: 714–723

I. INTRODUCTION

A spherical (surface/shell) array of uniformly[1] spaced isotropic[2] sensors offers a directionality that remains invariant over any polar/azimuthal rotation about the spherical origin. Physical implementations of a uniform spherical array of identical isotropic microphones/hydrophones are reported in Refs. 3–19 of which Refs. 5, 7, and 12–19 are commercial products. These hardware implementations are summarized in Table I.

Spherical arrays are often used for direction finding, for example, see Refs. 8, 10–13, and 20–58. The corresponding Cramér–Rao bound (CRB)[59] has been

(i) plotted in Refs. 32, 37, 39, 45, 48, 50, 53, 54, and 56 but without stating any mathematical derivation/expression for either the Fisher information matrix (FIM) or the Cramér–Rao bound.
(ii) expressed in only open forms in Refs. 12, 21, 35, 36, 41, and 51. The phrase "open form" here refers to mathematical expressions in terms of unsolved derivatives and/or integrals and/or infinite sums. That is, these references presented foundational mathematical expressions/formulas useful toward deriving the Fisher information matrix, which nonetheless remains not stated explicitly in terms of the data model's parameters.

Nevertheless, no *closed*-form expression is yet available in the open literature for any direction-finding Cramér–Rao bounds using a uniform spherical array of identical isotropic sensors. This paper is the first.

More importantly, this paper is the first in the open literature to propose the following rules-of-thumb for the design of an open sphere array:

(a) The polar arrival angle's CRB(θ) is approximately related to the system-design parameters via

$$2\pi\frac{R}{\lambda}\frac{\sigma_s}{\sigma_n}\sqrt{2LM\mathrm{CRB}(\theta)} \approx \sqrt{3} - (Le^{6/7})^{-1} \tag{1}$$

$$\underset{L\to\infty}{\longrightarrow} \sqrt{3}, \quad \forall(\theta,\phi). \tag{2}$$

This approximation and this convergence hold, rather remarkably, for all possible directions-of-arrival.

(b) The azimuth arrival angle's CRB(ϕ) is approximately related to the system-design parameters via

$$2\pi\frac{R}{\lambda}\frac{\sigma_s}{\sigma_n}\sin(\theta)\sqrt{2LM\mathrm{CRB}(\phi)} \approx \sqrt{3} + (Le^{1/14})^{-1} \tag{3}$$

$$\underset{L\to\infty}{\longrightarrow} \sqrt{3}, \quad \forall(\theta,\phi). \tag{4}$$

This approximation and this convergence hold for all potential angles-of-arrival. Here, M stands for the number of snapshots, R indicates the spherical radius, λ represents the incident signal's wavelength, and $(\sigma_s/\sigma_n)^2$ expresses the signal-to-noise power ratio. The rules-of-thumb in Eqs. (1)–(3) indicate to the system engineer how large a sphere (i.e., R/λ), how many sensors (L) and how many snapshots (M) would be required to satisfy a preset threshold of direction-finding precision (i.e., the CRB) under any signal-to-noise power ratio $(\sigma_s/\sigma_n)^2$. These closed-form formulas are obtained here based on statistical observations on the numerical behaviors of the derived Cramér–Rao bounds over all directions-of-arrival.

The rest of this paper is organized as follows: Sec. II defines the statistical data model. Section III derives the

a)Electronic mail: ktwong@ieee.org

TABLE I. Practical implementations of a uniform spherical array of isotropic sensors.

Name	Open sphere?	Commercial manufacturer	Number of microphones/ hydrophones	Radius	References
n.a.	Open	n.a.	8	13.9 cm	8
n.a.	Rigid	n.a.	16	2.5 cm	6
Eigen Mike	Rigid	mh acoustics LLC (New Jersey, USA)	32	4.2 cm	5, 12, 13
Eigen Mike	Rigid	n.a.	32	5 cm	11
Type 8606 spherical beamforming system	Rigid	Brüel & Kjær (Nærum, Denmark)	36	9.75 cm	14, 15
Type 8606 spherical beamforming system	Rigid	Brüel & Kjær (Nærum, Denmark)	36 or 50	9.75 cm	19
Generation I spherical array (NRL/NASA)	Rigid	n.a.	50	20 cm	4
Generation II (Boeing) array	Open	n.a.	50	20 cm	4
Type 8606 spherical beamforming system	Rigid	Brüel & Kjær (Nærum, Denmark)	50	9.75 cm	7
n.a.	Rigid	n.a.	64	9.75 cm	10
VisiSonics 5/64 audio visual camera	Rigid	VisiSonics (Maryland, USA)	64	10 cm	16
Sphere48-35 AC Pro	Open	Acoustic Camera (Berlin, Germany)	64	17.5 cm	17
Sphere120-60 AC Pro	Open	Acoustic Camera (Berlin, Germany)	120	30 cm	18
n.a.	Rigid	n.a.	252	8.5 cm	9
U.S. patent number 4203162	Rigid	n.a.	Hundreds to thousands	one to several yards	3

Cramér–Rao bounds. Section IV analyzes the statistical behaviors of the polar-angle CRB(θ) for small L and as $L \to \infty$. Section V does the same for the azimuth-angle CRB(ϕ). Section VI verifies the earlier derived Cramér–Rao bounds via Monte Carlo simulations of the maximum-likelihood estimator. Section VII concludes the entire investigation.

II. THE MEASUREMENT DATA MODEL

Consider L identical isotropic sensors, uniformly[60] placed on the surface of a sphere of radius R. Upon this spherical shell array, there impinges a signal $\{s(m), \forall m\}$ of wavelength λ, from the far field, at an incident polar angle of $\theta \in [0, \pi]$ and an azimuth angle of $\phi \in [0, 2\pi)$. Suppose the ℓth sensor positioned at the Cartesian coordinates of $[x_\ell, y_\ell, z_\ell] = [R\sin(\theta_\ell)\cos(\phi_\ell), R\sin(\theta_\ell)\sin(\phi_\ell), R\cos(\theta_\ell)]$, where (θ_ℓ, ϕ_ℓ) represents the ℓth sensor's location in the polar-azimuthal coordinates. See Fig. 1. The spherical array would thus have an $L \times 1$ array manifold $\mathbf{a}(\theta, \phi)$, whose ℓth entry equals $[\mathbf{a}(\theta, \phi)]_\ell = e^{j\kappa_\ell}$, where

$$\kappa_\ell = 2\pi\frac{R}{\lambda}\left[\sin(\theta)\sin(\theta_\ell)\cos(\phi - \phi_\ell) + \cos(\theta)\cos(\theta_\ell)\right]$$

represents the ℓth sensor's spatial phase factor.

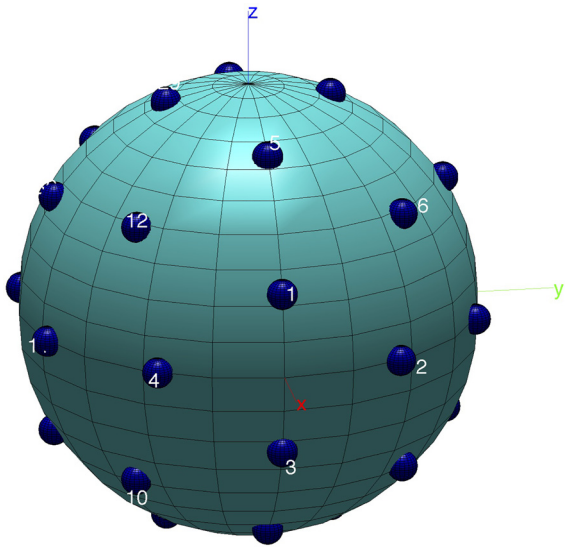

FIG. 1. (Color online) A uniform spherical array (USA) of isotropic sensors, with each sensor represented by a solid dot.

At the mth time instant, the entire spherical array collects an $L \times 1$ vector of data:

$$\mathbf{z}(m) = \mathbf{a}(\theta, \phi)s(m) + \mathbf{n}(m), \quad \text{for } m = 1, 2, \ldots, M, \tag{5}$$

where $\mathbf{n}(m)$ represents an $L \times 1$ vector of additive noise.

Here, the impinging signal is a complex-valued sinusoid of $s(m) = \sigma_s e^{j(2\pi fm + \psi)}$, $m = 1, 2, \ldots, M$, whose amplitude σ_s, frequency $f \in (0, 1)$, and initial phase $\psi \in (-\pi, \pi]$ are all prior known. The additive noise $\{\mathbf{n}(m), \forall m\}$ is complex-valued circularly symmetric Gaussian, with a prior known mean of zero, a prior known variance of σ_n^2, and a prior known spatio-temporal statistical independence. Furthermore, the signal and the noise are statistically not cross-correlated.

To concentrate on how the number (L) of identical isotropic sensors would affect the spherical *array*'s direction-finding Cramér–Rao bounds, this paper will use an admittedly simple statistical model of the incident *signal* and the corrupting *noise*. More complicated signal-and-noise scenarios could be handled handily, using the analytical approach in this paper, but would then bring distracting considerations that obscure the present focus on the number (L) of sensors in the spherical array.

With a total of M number of time samples, the entire dataset may be expressed as an $ML \times 1$ vector:

$$\overbrace{\begin{bmatrix}\mathbf{z}(1)\\ \vdots \\ \mathbf{z}(M)\end{bmatrix}}^{\tilde{\mathbf{z}} :=} = \overbrace{\begin{bmatrix}s(1)\\ \vdots \\ s(M)\end{bmatrix}}^{\mathbf{s} :=} \otimes \mathbf{a}(\theta, \phi) + \overbrace{\begin{bmatrix}\mathbf{n}(1)\\ \vdots \\ \mathbf{n}(M)\end{bmatrix}}^{\tilde{\mathbf{n}} :=}, \tag{6}$$

where $\otimes$ symbolizes the Kronecker product.

III. CRAMÉR–RAO BOUND DERIVATION

The above signal-and-noise data model implies that the dataset $\tilde{\mathbf{z}}$ has a probability density that is complex-valued circularly symmetric Gaussian:

$$p(\tilde{\mathbf{z}};\theta,\phi)=\frac{1}{|\pi\boldsymbol{\Gamma}|}\exp\left\{-[\tilde{\mathbf{z}}-\boldsymbol{\mu}]^H\boldsymbol{\Gamma}^{-1}[\tilde{\mathbf{z}}-\boldsymbol{\mu}]\right\}, \tag{7}$$

where

$$\begin{aligned}\boldsymbol{\mu} :&= E[\tilde{\mathbf{z}}]\\ &= \mathbf{s}\otimes\mathbf{a}(\theta,\phi)+E[\tilde{\mathbf{n}}]\\ &= \mathbf{s}\otimes\mathbf{a}(\theta,\phi)\end{aligned}$$

denotes the statistical mean, and

$$\begin{aligned}\boldsymbol{\Gamma} &:= \mathrm{cov}(\tilde{\mathbf{z}}) \qquad (8)\\ &= E_{\tilde{\mathbf{z}}}\{(\tilde{\mathbf{z}}-\boldsymbol{\mu})[\tilde{\mathbf{z}}-\boldsymbol{\mu}]^H\}\\ &= E[\tilde{\mathbf{n}}\tilde{\mathbf{n}}^H]\\ &= \sigma_n^2\mathbf{I}_{LM} \qquad (9)\end{aligned}$$

represents the data's covariance matrix. In the above, $\mathbf{I}_{LM}$ symbolizes an $LM\times LM$ identity matrix, and the superscript ^{H} signifies the Hermitian operator.

The only parameters to be estimated are θ and ϕ, which will be collected into a 2×1 vector of $\boldsymbol{\xi}=[\theta,\ \phi]^T$.

The $(i,\ j)$th element of the Fisher information matrix $\mathbf{F}(\boldsymbol{\xi})$ is given by [see (3.8) on p. 72 of Ref. 61]

$$\begin{aligned}[\mathbf{F}(\boldsymbol{\xi})]_{i,j} &= 2\mathrm{Re}\left[\left(\frac{\partial\boldsymbol{\mu}}{\partial\xi_i}\right)^H\boldsymbol{\Gamma}^{-1}\left(\frac{\partial\boldsymbol{\mu}}{\partial\xi_j}\right)\right]\\ &\quad+\mathrm{Tr}\left\{\boldsymbol{\Gamma}^{-1}\left(\frac{\partial\boldsymbol{\Gamma}}{\partial\xi_i}\right)\boldsymbol{\Gamma}^{-1}\left(\frac{\partial\boldsymbol{\Gamma}}{\partial\xi_j}\right)\right\}, \qquad (10)\end{aligned}$$

where ξ_i denotes the ith entry of the 2×1 vector $\boldsymbol{\xi}$. As $\boldsymbol{\Gamma}$ is functionally independent of $\boldsymbol{\xi}$,

$$[\mathbf{F}(\boldsymbol{\xi})]_{i,j}=2\mathrm{Re}\left[\left(\frac{\partial\boldsymbol{\mu}}{\partial\xi_i}\right)^H\boldsymbol{\Gamma}^{-1}\left(\frac{\partial\boldsymbol{\mu}}{\partial\xi_j}\right)\right].$$

From Eq. (9),

$$[\mathbf{F}(\boldsymbol{\xi})]_{i,j}=\frac{1}{\sigma_n^2}2\mathrm{Re}\left[\left(\frac{\partial\boldsymbol{\mu}}{\partial\xi_i}\right)^H\left(\frac{\partial\boldsymbol{\mu}}{\partial\xi_j}\right)\right]. \tag{11}$$

To express Eq. (11) explicitly in terms of the data model parameters, the following partial derivatives will be useful:

$$\frac{\partial\boldsymbol{\mu}}{\partial\theta}=\mathbf{s}\otimes\frac{\partial\mathbf{a}(\theta,\phi)}{\partial\theta}=\mathbf{s}\otimes\frac{j2\pi R}{\lambda}\begin{bmatrix}\big(\cos(\theta)\sin(\theta_1)\cos(\phi-\phi_1)-\cos(\theta_1)\sin(\theta)\big)e^{j\kappa_1}\\ \big(\cos(\theta)\sin(\theta_2)\cos(\phi-\phi_2)-\cos(\theta_2)\sin(\theta)\big)e^{j\kappa_2}\\ \vdots\\ \big(\cos(\theta)\sin(\theta_L)\cos(\phi-\phi_L)-\cos(\theta_L)\sin(\theta)\big)e^{j\kappa_L}\end{bmatrix},$$

$$\frac{\partial\boldsymbol{\mu}}{\partial\phi}=\mathbf{s}\otimes\frac{\partial\mathbf{a}(\theta,\phi)}{\partial\phi}=-\mathbf{s}\otimes j\frac{2\pi R}{\lambda}\sin(\theta)\begin{bmatrix}\sin(\theta_1)\sin(\phi-\phi_1)e^{j\kappa_1}\\ \sin(\theta_2)\sin(\phi-\phi_2)e^{j\kappa_2}\\ \vdots\\ \sin(\theta_L)\sin(\phi-\phi_L)e^{j\kappa_L}\end{bmatrix},$$

$$\frac{\partial[\mathbf{a}(\theta,\phi)]_\ell}{\partial\theta}=\frac{\partial\kappa_\ell}{\partial\theta}e^{j\kappa_\ell},$$

$$\frac{\partial[\mathbf{a}(\theta,\phi)]_\ell}{\partial\phi}=\frac{\partial\kappa_\ell}{\partial\phi}e^{j\kappa_\ell},$$

$$\frac{\partial\kappa_\ell}{\partial\theta}=2\pi\frac{R}{\lambda}\big[\cos(\theta)\sin(\theta_\ell)\cos(\phi-\phi_\ell)-\cos(\theta_\ell)\sin(\theta)\big],$$

$$\frac{\partial\kappa_\ell}{\partial\phi}=-2\pi\frac{R}{\lambda}\sin(\theta)\sin(\theta_\ell)\sin(\phi-\phi_\ell).$$

Denote the entries of $\mathbf{F}(\boldsymbol{\xi})$ as

$$\mathbf{F}(\boldsymbol{\xi})=\begin{bmatrix}F_{\theta,\theta} & F_{\theta,\phi}\\ F_{\phi,\theta} & F_{\phi,\phi}\end{bmatrix}.$$

Substitute the above partial derivatives into Eq. (11):

$$F_{\theta,\theta} = 2M\left(2\pi\frac{R}{\lambda}\frac{\sigma_s}{\sigma_n}\right)^2\sum_{\ell=1}^{L}\left[\cos(\theta)\sin(\theta_\ell)\cos(\phi-\phi_\ell) - \cos(\theta_\ell)\sin(\theta)\right]^2,$$

$$F_{\theta,\phi} = -2M\left(2\pi\frac{R}{\lambda}\frac{\sigma_s}{\sigma_n}\right)^2\sin(\theta)\sum_{\ell=1}^{L}\left[\sin(\theta_\ell)\sin(\phi-\phi_\ell)\left(\cos(\theta)\sin(\theta_\ell)\cos(\phi-\phi_\ell) - \cos(\theta_\ell)\sin(\theta)\right)\right] = F_{\phi,\theta},$$

$$F_{\phi,\phi} = 2M\left(2\pi\frac{R}{\lambda}\frac{\sigma_s}{\sigma_n}\sin(\theta)\right)^2\sum_{\ell=1}^{L}\left[\sin^2(\theta_\ell)\sin^2(\phi-\phi_\ell)\right].$$

The deterministic Cramér–Rao bounds (also known as the conditional Cramér–Rao bounds) of θ and ϕ equal the diagonal entries in

$$\begin{bmatrix} \mathrm{CRB}(\theta) & * \\ * & \mathrm{CRB}(\phi) \end{bmatrix}. = \mathbf{F}^{-1}(\boldsymbol{\xi}) = \frac{1}{F_{\theta,\theta}F_{\phi,\phi} - F_{\theta,\phi}^2}\begin{bmatrix} F_{\phi,\phi} & -F_{\theta,\phi} \\ -F_{\phi,\theta} & F_{\theta,\theta} \end{bmatrix}. \tag{12}$$

That is,

$$\mathrm{CRB}(\theta) = \frac{F_{\phi,\phi}}{F_{\theta,\theta}F_{\phi,\phi} - F_{\theta,\phi}^2} = \frac{1}{2M}\left(2\pi\frac{R}{\lambda}\frac{\sigma_s}{\sigma_n}\right)^{-2}\left\{\sum_{\ell=1}^{L}\left[\cos(\theta)\sin(\theta_\ell)\cos(\phi-\phi_\ell) - \cos(\theta_\ell)\sin(\theta)\right]^2 - \frac{\left\{\sum_{\ell=1}^{L}\left[\cos(\theta)\sin^2(\theta_\ell)\sin(2(\phi-\phi_\ell)) - \sin(\theta)\sin(2\theta_\ell)\sin(\phi-\phi_\ell)\right]\right\}^2}{4\sum_{\ell=1}^{L}\left[\sin^2(\theta_\ell)\sin^2(\phi-\phi_\ell)\right]}\right\}^{-1} \tag{13}$$

and

$$\mathrm{CRB}(\phi) = \frac{F_{\theta,\theta}}{F_{\theta,\theta}F_{\phi,\phi} - F_{\theta,\phi}^2} = \frac{1}{2M}\left(2\pi\frac{R}{\lambda}\frac{\sigma_s}{\sigma_n}\right)^{-2}\sin^{-2}(\theta)\left\{\left[\sum_{\ell=1}^{L}\sin^2(\theta_\ell)\sin^2(\phi-\phi_\ell)\right] - \frac{\left\{\sum_{\ell=1}^{L}\left[\cos(\theta)\sin^2(\theta_\ell)\sin(2(\phi-\phi_\ell)) - \sin(\theta)\sin(2\theta_\ell)\sin(\phi-\phi_\ell)\right]\right\}^2}{4\sum_{\ell=1}^{L}\left[\cos(\theta)\sin(\theta_\ell)\cos(\phi-\phi_\ell) - \cos(\theta_\ell)\sin(\theta)\right]^2}\right\}^{-1}. \tag{14}$$

The above equations have expressed the azimuth-polar bivariate direction-of-arrival Cramér–Rao bounds in closed forms, explicitly in terms of the data-model parameters.

IV. RULE-OF-THUMB ARRAY-DESIGN FORMULA RELATING CRB(θ) TO L

Referring to the right side of Eq. (13), the expression $\sqrt{2LM\mathrm{CRB}(\theta)}(2\pi(R/\lambda)(\sigma_s/\sigma_n))$ has only three degrees-of-freedom (namely, θ, ϕ, L) apart from the sensors' locations.

A. How CRB(θ) varies with θ and with ϕ

This expression of $\sqrt{2LM\mathrm{CRB}(\theta)}(2\pi(R/\lambda)(\sigma_s/\sigma_n))$ is plotted in Fig. 2 versus θ and ϕ, at various values of L. Some qualitative observations:

(a) The expression varies little with the azimuth angle ϕ, for a sufficiently large L. This is because as L increases, the sensors become more evenly distributed with respect to ϕ.

(b) The expression decreases (i.e., improves) as θ increases (i.e., as the incident source becomes more horizontal). Nonetheless, whatever variation here becomes effectively negligible as L increases. This leads to Sec. IV B below.

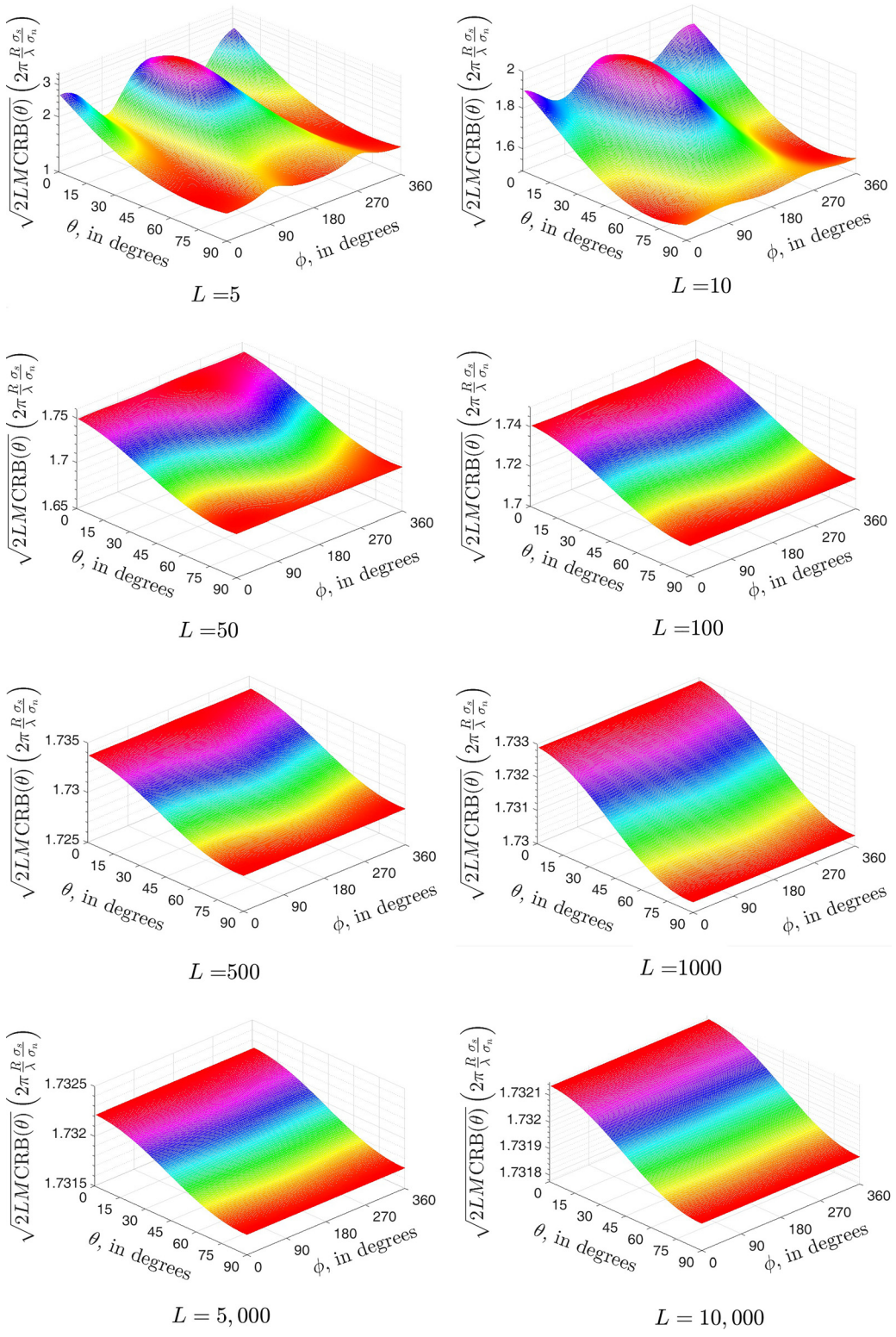

FIG. 2. (Color online) $\sqrt{2LM\mathrm{CRB}(\theta)}[2\pi(R/\lambda)(\sigma_s/\sigma_n)]$ of Eq. (13) plotted versus (θ, ϕ), at various L. Note how the vertical range shrinks, as L increases across the subfigures.

B. How *L*CRB(θ) varies with *L*

The population $\mathcal{C}_\theta^{(L)} := \{\sqrt{2LM\mathrm{CRB}(\theta)}(2\pi(R/\lambda)(\sigma_s/\sigma_n)), \forall(\theta,\phi)\}$ takes on numerical values that lie entirely within a dynamic range that shrinks progressively as L increases. To facilitate the subsequent discussions: denote as $\mu_\theta^{(L)}$ the algebraic average of the population $\mathcal{C}_\theta^{(L)}$ at L; signify as $\sigma_\theta^{(L)}$ the standard deviation of $\mathcal{C}_\theta^{(L)}$ at L. At $L = 600$: the dynamic range tightens to [1.729, 1.734] with a thin width of only 0.005 and a miniscure $\sigma_\theta^{(600)} \approx 1.53 \times 10^{-3}$; that is, the entire population $\mathcal{C}_\theta^{(600)}$ (defined over all (θ, ϕ)) has effectively converged to a scalar constant of $\mu_\theta^{(600)} = 1.731 \approx \sqrt{3}$, where the approximation is to within three significant figures.

A natural question: At other values of L, could the entire $\mathcal{C}_\theta^{(L)}$ be represented as the single scalar of $\mu_\theta^{(L)}$? Figure 3 addresses this issue by plotting the dynamic range of $\mathcal{C}_\theta^{(L)}$, the scalar $\mu_\theta^{(L)}$, and the scalars $\mu_\theta^{(L)} \pm \sigma_\theta^{(L)}$, each versus L. There, $\mathcal{C}_\theta^{(L)}$ does appear to converge to $\mu_\theta^{(L)}$ for a sufficiently large L.

An immediate follow-up question: How then does $\mu_\theta^{(L)}$ vary with L? To answer this question, Fig. 4 plots $\sqrt{3} - \mu_\theta^{(L)}$ versus L, as a two-dimensional graph in $\log_e$–$\log_e$ scale; the relationship appears graphically linear-like. A least-squares fit of $\log_e(\sqrt{3} - \mu_\theta^{(L)})$ versus $\log_e(L)$ leads to

$$\log_e(\sqrt{3} - \mu_\theta^{(L)}) \approx -0.8517 - 0.9940 \log_e(L)$$
$$\Rightarrow \mu_\theta^{(L)} \approx \sqrt{3} - L^{-0.9940} e^{-0.8517}, \tag{15}$$

with a root-mean-square error of only 0.00923 in the $\log_e$–$\log_e$ scale. The 0.8517 in Eq. (15) is approximately $6/7$ (precise to within two significant figures); similarly, $0.9940 \approx 1$ (precise to within two significant figures). Hence, the linear relationship in Eq. (15) may be further approximated into an elegant form of

$$\log_e\left(\sqrt{3} - \mu_\theta^{(L)}\right) \approx -\frac{6}{7} - \log_e(L), \tag{16}$$

which incurs a root-mean-square fitting error of 0.04612 (in the $\log_e$–$\log_e$ scale). This Eq. (16) may be re-expressed as

$$\mu_\theta^{(L)} \approx \sqrt{3} - \frac{1}{L} e^{-(6/7)}. \tag{17}$$

Yet another question: If the entire set $\mathcal{C}_\theta^{(L)}$ roughly converges to the scalar $\mu_\theta^{(L)}$ of Eq. (17), what is the root-mean-square error thus incurred at each L? This is answered quantitatively in Fig. 5.

V. RULE-OF-THUMB ARRAY-DESIGN FORMULA RELATING CRB(ϕ) TO L

The right side of Eq. (14) indicates that $\sqrt{2LM\mathrm{CRB}(\phi)}(2\pi(R/\lambda)(\sigma_s/\sigma_n)\sin(\theta))$ has only three degrees-of-freedom (namely, θ, ϕ, L) apart from the sensors' locations.

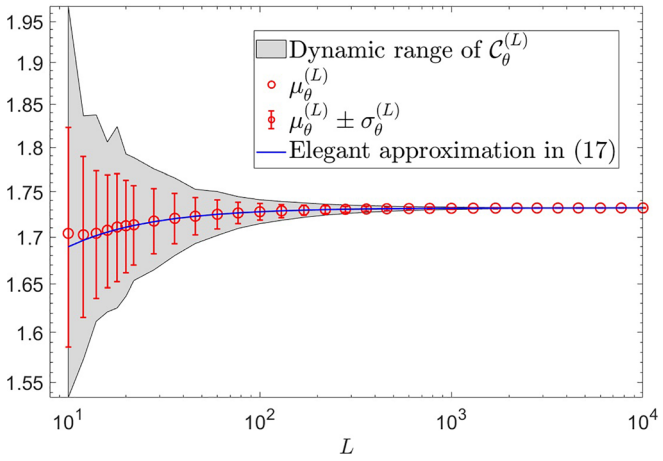

FIG. 3. (Color online) The shrinking dynamic range of $\mathcal{C}_\theta^{(L)}$ as L increases.

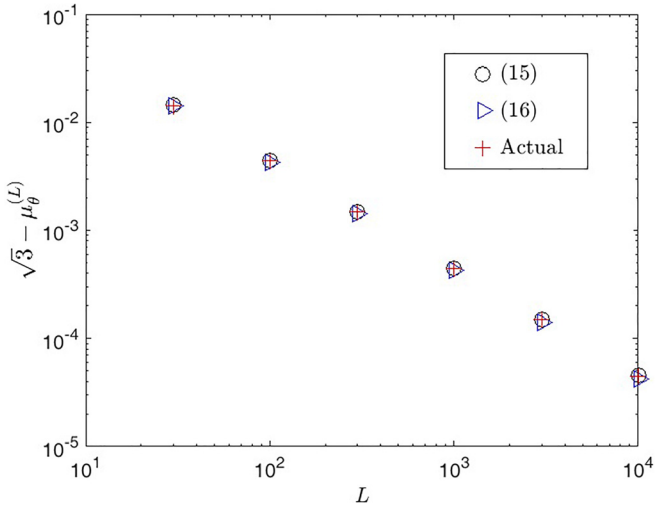

FIG. 4. (Color online) $(\sqrt{3} - \mu_\theta^{(L)})$—its actual value, and its approximations in Eqs. (15) and (16).

A. How CRB(ϕ) *sin*(θ) varies with θ and with ϕ

The expression $\sqrt{2LM\mathrm{CRB}(\phi)}(2\pi(R/\lambda)(\sigma_s/\sigma_n)\sin(\theta))$ is plotted in Fig. 6 versus (θ, ϕ) at various L. Some qualitative observations thereof:

(a) This expression varies little with the polar angle θ, especially for a sufficiently large L. In other words, CRB(ϕ) [without multiplication by $\sin^2(\theta)$] would approach infinity as $\theta \to 0, \pi$. This observation has earlier been made in Refs. 21 (pp. 17–18), 56 (p. 186), and 58 (p. 82).

(b) This expression varies sinusoidally with ϕ, with a period of 180°. This sinusoidal variation is on account of the terms $\sin(2(\phi - \phi_\ell))$, $\sin(\phi - \phi_\ell)$, and $\cos(\phi - \phi_\ell)$ in Eq. (14).

B. How CRB (ϕ) *sin*(θ) varies with *L*

The population $\mathcal{C}_\phi^{(L)} := \{\sqrt{2LM\mathrm{CRB}(\phi)}(2\pi(R/\lambda)(\sigma_s/\sigma_n)\sin(\theta)), \forall(\theta, \phi)\}$ takes on numerical values that lie entirely within a dynamic range which shrinks progressively as L increases. As before, denote as $\mu_\phi^{(L)}$ the algebraic average of the population $\mathcal{C}_\phi^{(L)}$ at L; use $\sigma_\phi^{(L)}$ to symbolize the

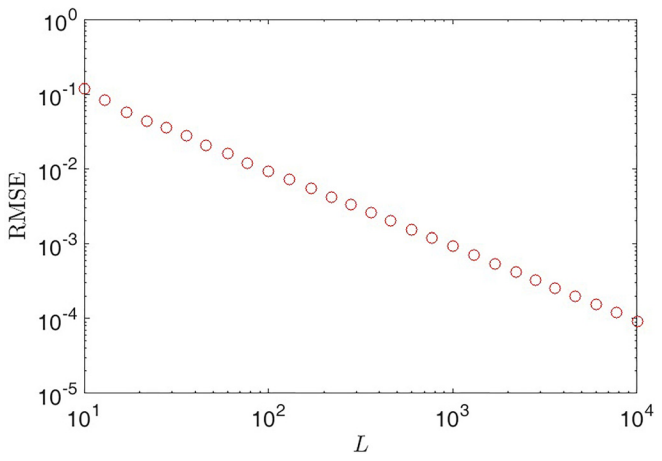

FIG. 5. (Color online) The RMSE of $\mathcal{C}_\theta^{(L)}$ with respect to Eq. (17).

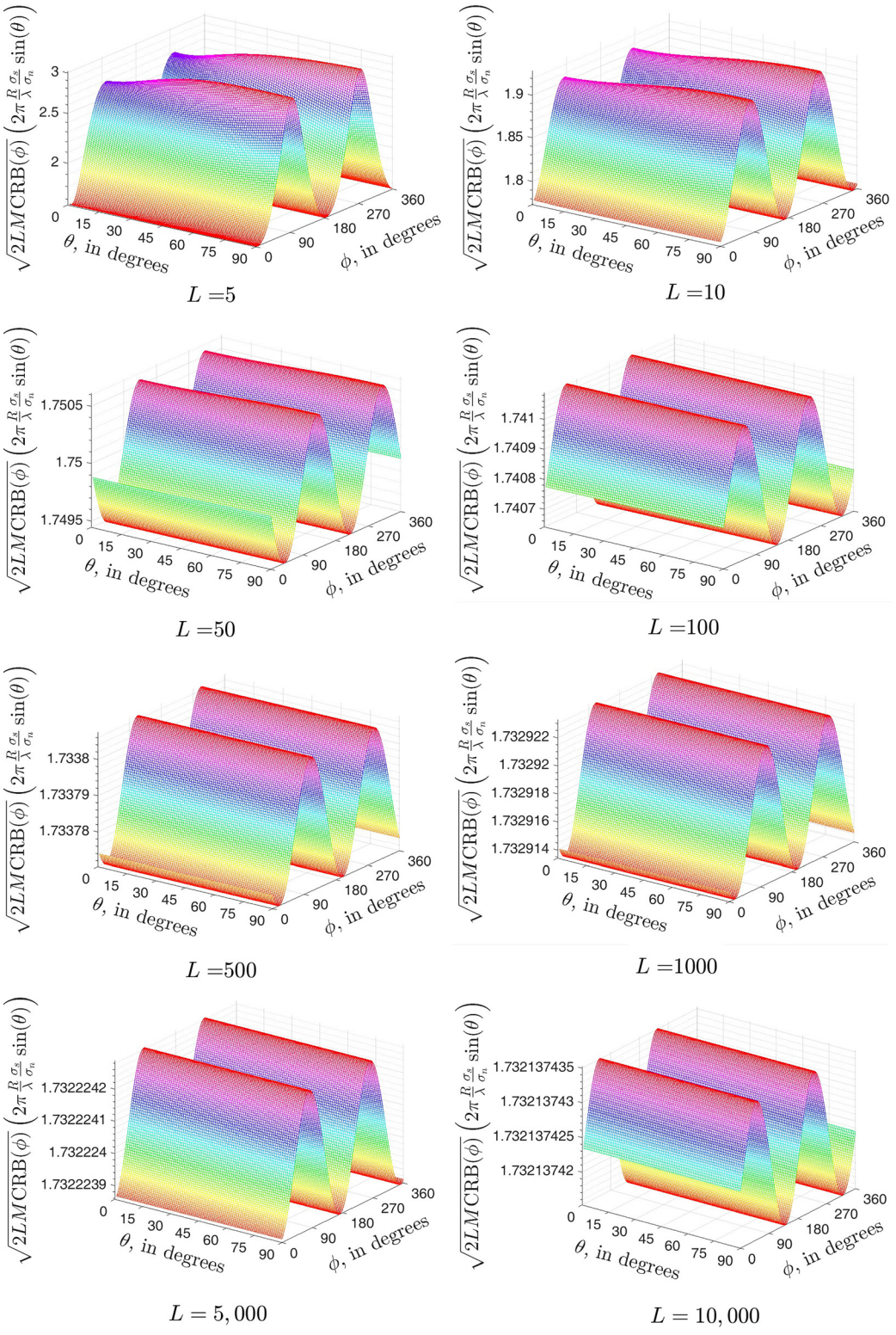

FIG. 6. (Color online) $\sqrt{2LM\mathrm{CRB}(\phi)}(2\pi(R/\lambda)(\sigma_s/\sigma_n)\sin(\theta))$ of Eq. (14) plotted versus θ and versus ϕ, at various values of L.

standard deviation of $\mathcal{C}_\phi^{(L)}$ at L. At $L=600$: the dynamic range narrows to [1.733 494, 1.733 503] with a slim width of only 9.31×10^{-6} and a negligible $\sigma_\phi^{(600)}\approx 3.29\times10^{-6}$; that is, the entire set $\mathcal{C}_\phi^{(600)}$ has effectively converged to a single constant scalar of $\mu_\phi^{(600)}=1.733\,498$ which approximates to $\sqrt{3}$ within three significant figures.

To investigate whether the entire population $\mathcal{C}_\phi^{(L)}$ (at what L) effectively converges to the one scalar of $\mu_\phi^{(L)}$, Fig. 7 plots the dynamic range of $\mathcal{C}_\phi^{(L)}$, the scalar of $\mu_\phi^{(L)}$, and the scalars of $\mu_\phi^{(L)}\pm\sigma_\phi^{(L)}$, each versus L. There, the population $\mathcal{C}_\phi^{(L)}$ seems to converge to $\mu_\phi^{(L)}$ for a sufficiently large L.

Next question: How does $\mu_\phi^{(L)}$ vary with L? To address this question, Fig. 8 plots $\mu_\phi^{(L)}-\sqrt{3}$ versus L, in the $\log_e$–$\log_e$ scale. A least-squares fit of $\log_e(\mu_\phi^{(L)}-\sqrt{3})$ versus $\log_e(L)$ leads to a straight line:

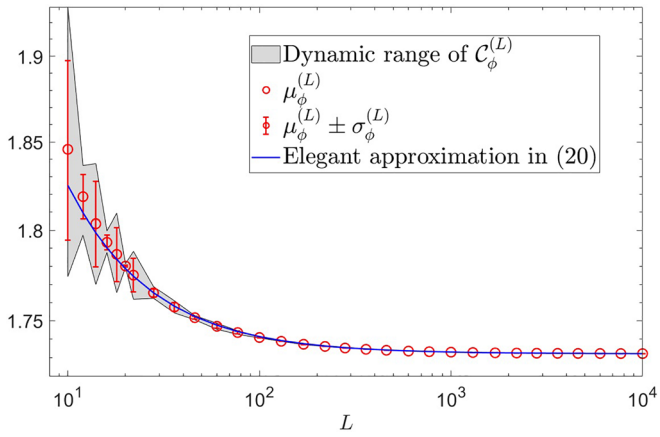

FIG. 7. (Color online) The shrinking dynamic range of $\mathcal{C}_\phi^{(L)}$ as L increases.

$$\log_e(\mu_\phi^{(L)} - \sqrt{3}) \approx -0.0722 - 1.009\log_e(L)$$
$$\Rightarrow \mu_\phi^{(L)} \approx \sqrt{3} + L^{1.0090}e^{-0.0722}, \tag{18}$$

with a root-mean-square error of only 0.0129 (in $\log_e$–$\log_e$ scale).

The linear relationship in Eq. (18) above may be approximated further into an elegant form of

$$\log_e\left(\mu_\phi^{(L)} - \sqrt{3}\right) \approx -\frac{1}{14} - \log_e(L), \tag{19}$$

with a root-mean-square error (over the six above-specified values of L) of 0.0618 (in $\log_e$–$\log_e$ scale). This Eq. (19) may be re-written as

$$\mu_\phi^{(L)} \approx \sqrt{3} - \frac{1}{L}e^{-(1/14)}. \tag{20}$$

Representing the entire population $\mathcal{C}_\phi^{(L)}$ only via the scalar $\mu_\phi^{(L)}$ of Eq. (20), the root-mean-square error incurred at each L is plotted in Fig. 9.

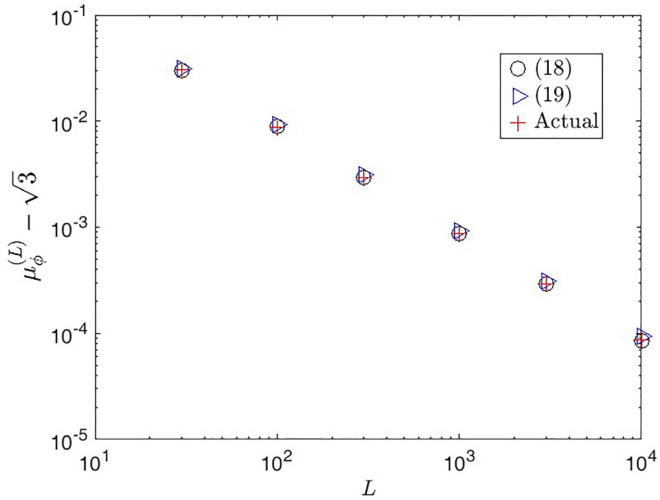

FIG. 8. (Color online) $(\mu_\phi^{(L)} - \sqrt{3})$—its actual values and its approximations in Eqs. (18) and (19).

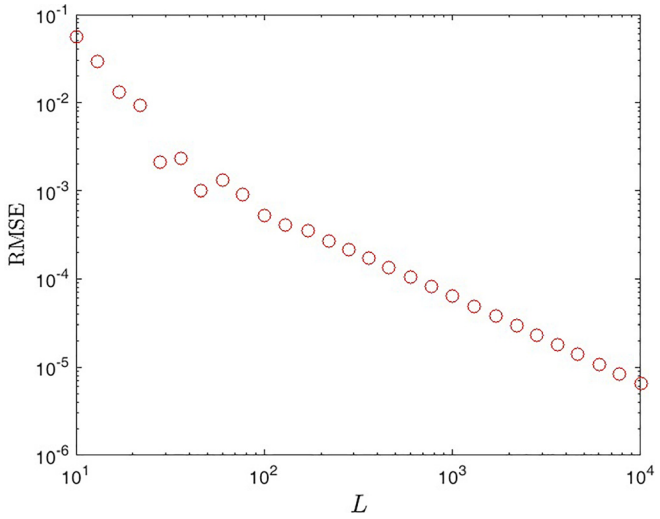

FIG. 9. (Color online) RMSE of $\mathcal{C}_\phi^{(L)}$ with respect to Eq. (20).

VI. VERIFICATION OF THE DERIVED CRBs VIA MAXIMUM LIKELIHOOD ESTIMATION

The Cramér–Rao bound is well known to be reached by the maximum-likelihood estimator (MLE). Hence, the former's correctness could be verified by the latter, as will be achieved in this section.

From $\tilde{\mathbf{z}} \sim \mathbb{C}N_{LM}(\boldsymbol{\mu}, \boldsymbol{\Gamma})$, the corresponding likelihood function equals

$$\mathcal{L}(\theta,\phi|\tilde{\mathbf{z}}_1,\ldots,\tilde{\mathbf{z}}_n) = \prod_{m=1}^{M}\frac{1}{|\pi\boldsymbol{\Gamma}|}\exp\left\{-[\tilde{\mathbf{z}}_m-\boldsymbol{\mu}]^T\boldsymbol{\Gamma}^{-1}[\tilde{\mathbf{z}}_m-\boldsymbol{\mu}]\right\}$$
$$= |\pi\boldsymbol{\Gamma}|^{-n}\exp\left\{-\sum_{k=1}^{M}[\tilde{\mathbf{z}}_m-\boldsymbol{\mu}]^T\boldsymbol{\Gamma}^{-1}[\tilde{\mathbf{z}}_m-\boldsymbol{\mu}]\right\}. \tag{21}$$

The maximum-likelihood estimators are (by definition)

$$(\hat{\theta}_{\text{MLE}}, \hat{\phi}_{\text{MLE}}) := \arg\max_{(\theta,\phi)} \mathcal{L}(\theta,\phi|\tilde{\mathbf{z}}_1,\ldots,\tilde{\mathbf{z}}_n)$$
$$= \arg\min_{(\theta,\phi)}\left\{\sum_{k=1}^{n}[\tilde{\mathbf{z}}_k-\boldsymbol{\mu}]^T\boldsymbol{\Gamma}^{-1}[\tilde{\mathbf{z}}_k-\boldsymbol{\mu}]\right\}. \tag{22}$$

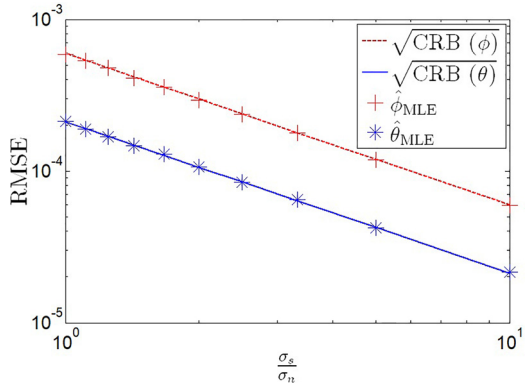

FIG. 10. (Color online) The maximum-likelihood estimates attain the derived Cramér–Rao bounds. Here, $L=10$, $R=1$, $\lambda=0.0344$, $f=0.25$, $\psi=0.23\pi$, $\theta=23°$, and $\phi=73°$.

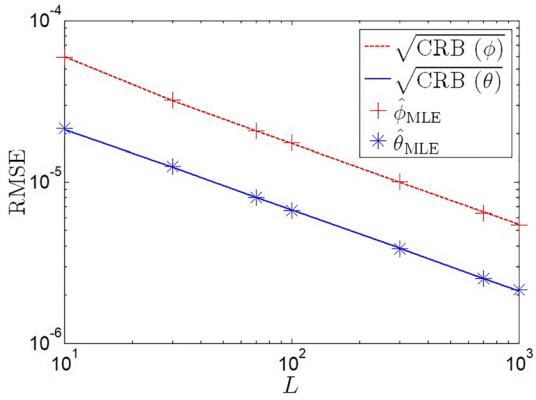

FIG. 11. (Color online) The maximum-likelihood estimates attain the derived Cramér–Rao bounds. Here, $\sigma_s/\sigma_n = 10$, $R = 1$, $\lambda = 0.0344$, $f = 0.25$, $\psi = 0.23\pi$, $\theta = 23°$, and $\phi = 73°$.

The above estimators are Monte Carlo simulated; their root-mean-square errors (RMSE)[62] are presented in Figs. 10 and 11. Each icon thereon consists of 4000 independent Monte Carlo experiments, each involves $M = 100$, snapshots.

Figures 10 and 11 do demonstrate excellent agreement of the maximum-likelihood estimation error with the Cramér–Rao bounds. These maximum-likelihood estimates of the polar and azimuth angles attain the Cramér–Rao bounds derived in Eqs. (13) and (14).

VII. CONCLUSIONS

This paper has advanced two elegantly simple rules-of-thumb in Eqs. (17) and (20), to aid the system development of an open spherical array for source localization, by interrelating how many isotropic sensors are to be placed uniformly on a sphere of what preset radius (R/λ) for an acceptable threshold of direction-finding precision (CRB(θ), CRB(ϕ)), under any particular signal-to-noise power ratio $(\sigma_s/\sigma_n)^2$ and with any preset number of snapshots M. The above rules-of-thumb are discovered from a new statistical analysis of the direction-finding Cramér–Rao bounds derived here.

ACKNOWLEDGMENT

The authors would like to thank Professor Charles Hung Lee and Dr. Andriy Olenko for useful discussions.

[1]"Uniformly spaced" means that the neighbouring sensors are equi-distant from each other, with distance defined on the surface of the sphere. This is the uniform sampling used in Refs. 5, 11–13, 24, 25, 27, 30, 34, 39–41, 49, and 57, and also in the present work.

[2]The term "isotropic" refers to the sensor's equal sensitivity to the incident signal regardless of the signal's polar-azimuth direction-of-arrival (θ, ϕ).

[3]W. L. Clearwaters, L. T. Einstein, P. F. Radics, Jr., and J. W. Soderberg, "Electrically steerable spherical hydrophone array," U.S. patent number 4203162 (May 13, 1980).

[4]B. J. Sklanka, J. R. Tuss, R. D. Buehrle, J. Klos, E. G. Williams, and N. Valdivia, "Acoustic source localization in aircraft interiors using microphone array technologies," in *AIAA/CEAS Aeroacoustics Conference* (2006), pp. 2006–2714.

[5]M. Binelli, A. Venturi, A. Amendola, and A. Farina, "Experimental analysis of spatial properties of the sound field inside a car employing a spherical microphone array," in *Audio Engineering Society Convention* (2011), p. 8338.

[6]S. Clapp, A. Guthrie, J. Braasch, and N. Xiang, "Three-dimensional spatial analysis of concert and recital halls with a spherical microphone array," in Proc. Mtgs. Acoust. **19**, 015020 (2013).

[7]E. Tiana-Roig, A. Torras-Rosell, E. Fernandez-Grande, C.-H. Jeong, and F. T. Agerkvist, "Enhancing the beamforming map of spherical arrays at low frequencies using acoustic holography," in *Berlin Beamforming Conference* (2014), pp. 1–14.

[8]Y. Hu, J. Lu, and X. Qiu, "A maximum likelihood direction of arrival estimation method for open-sphere microphone arrays in the spherical harmonic domain," J. Acoust. Soc. Am. **138**(2), 791–794 (2015).

[9]S. Sakamoto, S. Hongo, T. Okamoto, Y. Iwaya, and Y. Suzuki, "Sound-space recording and binaural presentation system based on a 252-channel microphone array," Acoust. Sci. Technol. **36**(6), 516–526 (2015).

[10]E. Fernandez-Grand and A. Xenaki, "Compressive sensing with a spherical microphone array," J. Acoust. Soc. Am. **139**(2), EL45–EL49 (2016).

[11]M. R. Bai, Y. H. Yao, C. S. Lai, and Y. Y. Lo, "Design and implementation of a space domain spherical microphone array with application to source localization and separation," J. Acoust. Soc. Am. **139**(3), 1058–1070 (2016).

[12]L. Kumar and R. M. Hedge, "Near-field acoustic source localization and beamforming in spherical harmonics domain," IEEE Trans. Signal Process. **64**(13), 3351–3361 (2016).

[13]L. Kumar, G. Bi, and R. M. Hedge, "The spherical harmonics root-MUSIC," in *IEEE International Conference on Acoustics, Speech and Signal Processing* (2016), pp. 3046–3050.

[14]Z. Chu, Y. Yang, and L. Shen, "Resolution and quantification accuracy enhancement of functional delay and sum beamforming for three-dimensional acoustic source identification with solid spherical arrays," Mech. Syst. Signal Process. **88**, 274–289 (2017).

[15]Y. Yang, Z. Chu, L. Shen, G. Ping, and Z. Xu, "Fast Fourier-based deconvolution for three-dimensional acoustic source identification with solid spherical arrays," Mech. Syst. Signal Process. **107**, 183–201 (2018).

[16]VisiSonics 5-64 audio visual camera, product manual available at http://visisonics.com/download/audiovisual-camera-pamphlet/ (Last viewed 23 July 2018).

[17]Array sphere 48-35 AC pro, product manual available at https://www.acoustic-camera.com/en/products/microphone-arrays/sphere48-35-ac-pro.html (Last viewed 23 July 2018).

[18]Array sphere 120-60 AC pro, product manual available at https://www.acoustic-camera.com/en/products/microphone-arrays/sphere120-60-ac-pro.html (Last viewed 23 July 2018).

[19]Spherical beamforming system type 8606, product manual available at https://www.bksv.com/media/doc/bn0690.pdf (Last viewed 23 July 2018).

[20]M. Mokhtar, A. Gamil, H. El-Henawy, and S. El-Ramly, "Arbitrary spherical array in superresolution direction finding systems," IEEE Natl. Radio Sci. Conf. **1**, 97–104 (2001).

[21]S. Nordebo and M. Gustafsson, "Fundamental limitations for DOA estimation by a sphere," Technical Report LUTEDX/(TEAT-7128), Lund University, Lund, Sweden, 2004.

[22]A. M. Kamath and B. L. Hughes, "Impact of vector antennas on direction estimation using a spherical array," in *IEEE Asilomar Conference on Signals, Systems and Computers* (2005), pp. 1702–1706.

[23]R. Goossens and H. Rogier, "Unitary spherical ESPRIT: 2-D angle estimation with spherical arrays for scalar fields," IET Signal Process. **3**(3), 221–231 (2009).

[24]X. Li, S. Yan, X. Ma, and C. Hou, "Spherical harmonics MUSIC versus conventional MUSIC," Appl. Acoust. **72**(9), 646–652 (2011).

[25]H. Sun, E. Mabande, K. Kowalczyk, and W. Kellermann, "Localization of distinct reflections in rooms using spherical microphone array eigenbeam processing," J. Acoust. Soc. Am. **131**(4), 2828–2840 (2012).

[26]Q. Huang and T. Song, "DOA estimation of mixed near-field and far-field sources using spherical array," in *IEEE International Conference on Signal Processing* (2012), pp. 382–385.

[27]E. Mabande, K. Kowalczyk, H. Sun, and W. Kellermann, "Room geometry inference based on spherical microphone array eigenbeam processing," J. Acoust. Soc. Am. **134**(4), 2773–2789 (2013).

[28]T. Noohi, N. Epain, and C. T. Jin, "Direction of arrival estimation for spherical microphone arrays by combination of independent component analysis and sparse recovery," in *IEEE International Conference on Acoustics, Speech and Signal Processing* (2013), pp. 346–349.

[29]D. P. Jarrett, E. A. P. Habets, and P. A. Naylor, "Spherical harmonic domain noise reduction using an MVDR beamformer and DOA-based

second-order statistics estimation," in *IEEE International Conference on Acoustics, Speech and Signal Processing* (2013), pp. 654–658.
[30]L. Kumar, K. Singhal, and R. M. Hegde, "Robust source localization and tracking using MUSIC-Group delay spectrum over spherical arrays," in *IEEE International Workshop on Computational Advances in Multi-Sensor Adaptive Processing* (2013), pp. 304–307.
[31]D. P. Jarrett, M. Taseska, E. A. P. Habets, and P. A. Naylor, "Noise reduction in the spherical harmonic domain using a tradeoff beamformer and narrowband DOA estimates," IEEE/ACM Trans. Audio, Speech Lang. Process. **22**(5), 967–978 (2014).
[32]Q. Huang and T. Wang, "Acoustic source localization in mixed field using spherical microphone arrays," IEEE EURASIP J. Adv. Signal Process. **90**(1), 1–16 (2014).
[33]Y. Xie, C. Peng, X. Jiang, and S. Ouyang, "Hardware design and implementation of DOA estimation algorithms for spherical array antennas," in *IEEE International Conference on Signal Processing, Communications and Computing* (2014), pp. 219–223.
[34]K. Singhal and R. M. Hegde, "A sparse reconstruction method for speech source localization using partial dictionaries over a spherical microphone array," in *Annual Conference of the International Speech Communication Association* (2014), pp. 2209–2213.
[35]L. Kumar and R. M. Hegde, "Stochastic Cramér-Rao bound analysis for DOA estimation in spherical harmonics domain," IEEE Signal Process. Lett. **22**(8), 1030–1034 (2015).
[36]Q. Huang, R. Hu, and Y. Fang, "Real-valued MVDR beamforming using spherical arrays with frequency invariant characteristic," Digital Signal Process. **48**, 239–245 (2016).
[37]Q. Huang, G. Zhang, and K. Liu, "Near-field source localization using spherical microphone arrays," Chin. J. Electron. **25**(1), 159–166 (2016).
[38]F. Wang and X. Pan, "Acoustic sources localization in 3D using multiple spherical arrays," J. Electr. Eng. Technol. **11**(3), 759–768 (2016).
[39]Q. Huang, G. Zhang, and Y. Fang, "Real-valued DOA estimation for spherical arrays using sparse Bayesian learning," Signal Process. **125**, 79–86 (2016).
[40]S. Tervo, "Single snapshot detection and estimation of reflections from room impulse responses in the spherical harmonic domain," IEEE/ACM Trans. Audio, Speech, Lang. Process. **24**(12), 2466–2480 (2016).
[41]L. Zhang, Q. Huang, and Y. Fang, "Conditional and unconditional CRB of DOA estimation in spherical harmonics domain," in *IEEE International Conference on Signal Processing* (2016), pp. 424–428.
[42]X. Pan, H. Wang, F. Wang, and C. Song, "Multiple spherical arrays design for acoustic source localization," in *IEEE Sensor Signal Processing for Defence* (2016).
[43]W. Gao, H. Zhao, and W. Xu, "Direction of arrival estimation based on spherical harmonics decomposition," *IEEE OCEANS Conference* (2016).
[44]A. H. Moore, C. Evers, and P. A. Naylor, "Direction of arrival estimation in the spherical harmonic domain using subspace pseudointensity vectors," IEEE/ACM Trans. Audio, Speech Lang. Process. **25**(1), 178–192 (2017).
[45]Q. Huang, G. Zhang, L. Xiang, and Y. Fang, "Unitary transformations for spherical harmonics MUSIC," Signal Process. **131**, 441–446 (2017).
[46]H. Morgenstern, B. Rafaely, and M. Noisternig, "Design framework for spherical microphone and loudspeaker arrays in a multiple-input multiple-output system," J. Acoust. Soc. Am. **141**(3), 2024–2038 (2017).
[47]J. J. Embrechts, "DOA (direction of arrival) estimation of incident sound waves on a spherical microphone array: Comparison of some correction methods proposed to solve the DOA bias," J. Acoust. Soc. Am. **141**(5), 3985 (2017).
[48]Q. Huang, L. Xiang, and K. Liu, "Off-grid DOA estimation in real spherical harmonics domain using sparse Bayesian inference," Signal Process. **137**, 124–134 (2017).
[49]S. Hafezi, A. H. Moore, and P. A. Naylor, "Augmented intensity vectors for direction of arrival estimation in the spherical harmonic domain," IEEE/ACM Trans. Audio, Speech Lang. Process. **25**(10), 1956–1968 (2017).
[50]Q. Huang, L. Zhang, and Y. Fang, "Two-stage decoupled DOA estimation based on real spherical harmonics for spherical arrays," IEEE/ACM Trans. Audio, Speech Lang. Process. **25**(11), 2045–2058 (2017).
[51]H. Lolaee and M. A. Akhaee, "Robust expectation-maximization algorithm for DOA estimation of acoustic sources in the spherical harmonic domain," arXiv:1711.01583 (November 2017).
[52]V. Varanasi and R. Hedge, "Robust online direction of arrival estimation using low dimensional spherical harmonic features," in *IEEE International Conference on Acoustics, Speech and Signal Processing* (2017), pp. 511–515.
[53]L. Zhang, Q. Huang, J. Huang, and Y. Fang, "A two-stage method for DOA estimation using spherical arrays," in *IEEE Region 10 Conference* (2017), pp. 2415–2420.
[54]L. Zhang, Q. Huang, K. Liu, and Y. Fang, "Wideband DOA estimation in spherical harmonic domain using sparse Bayesian learning," in *IEEE Chinese Control Conference* (2017), pp. 5183–5187.
[55]S. Hafezi, A. H. Moore, and P. A. Naylor, "Multiple DOA estimation based on estimation consistency and spherical harmonic multiple signal classification," in *IEEE European Signal Processing Conference* (2017), pp. 1240–1244.
[56]B. Jo and J. W. Choi, "Direction of arrival estimation using nonsingular spherical ESPRIT," J. Acoust. Soc. Am. **143**(3), EL181–EL187 (2018).
[57]X. Pan, H. Wang, Z. Lou, and Y. Su, "Fast direction-of-arrival estimation algorithm for multiple wideband acoustic sources using multiple open spherical arrays," Appl. Acoust. **136**, 41–47 (2018).
[58]L. Zuo, J. Pan, and B. Ma, "Fast DOA estimation in the spectral domain and its applications," Progr. Electromagn. Res. **66**, 73–85 (2018).
[59]Any unbiased estimator's estimation-error variance could not fall below (i.e., outperform) the Cramér–Rao lower bound (given any specified model of the data's statistics). Hence, the Cramér–Rao bound is useful in the development of the measurement system and of the associated estimation algorithms, to see how much reduction in the estimation error variance could be obtainable by using a more expensive measurement system and/or a more complicated estimation algorithm.
[60]The uniform positioning of the sensors on the sphere is via the spiral sampling algorithm (Ref. 63), for which the MATLAB codes are available in Ref. 64.
[61]F. Castanie, *Digital Spectral Analysis: Parametric, Non-Parametric and Advanced Methods* (Wiley, Hoboken, NJ, 2011).
[62]The root-mean-square error (RMSE) is defined as RMSE $= \sqrt{\frac{1}{4000}\sum_{k=1}^{4000}\left(\hat{\theta}_{\mathrm{MLE},k}-\theta\right)^2}$ for the polar angle and RMSE $= \sqrt{\frac{1}{4000}\sum_{k=1}^{4000}\left(\hat{\phi}_{\mathrm{MLE},k}-\phi\right)^2}$ for the azimuth angle where $(\hat{\theta}_{\mathrm{MLE},k}, \hat{\phi}_{\mathrm{MLE},k})$ represents the kth Monte Carlo experiment maximum-likelihood arrival angle estimate.
[63]C. Carlson, "How I made wine glasses from sunflowers," Wolfram Blog, 2011, available at http://blog.wolfram.com/2011/07/28/how-i-made-wine-glasses-from-sunflowers/ (Last viewed 13 March 2018).
[64]A. Semechko, "Suites of functions to perform uniform sampling of sphere," MathWorks File Exchange, 2015, available at https://www.mathworks.com/matlabcentral/fileexchange/37004-suite-of-functions-to-perform-uniform-sampling-of-a-sphere (Last viewed 13 March 2018).